
Deep Near-infrared Imaging Observation of the Faint X-ray Point Sources Constituting the Galactic Bulge X-ray Emission

Kumiko MORIHANA,^{1,2} Masahiro TSUJIMOTO,³ Ken EBISAWA,³ and Poshak Gandhi⁴

¹Graduate School of Science, Nagoya University, Chikusa-ku, Nagoya, Aichi 464-8602, Japan

²Institute of Liberal Arts and Sciences, Nagoya University, Chikusa-ku, Nagoya, Aichi 464-8601, Japan

³Japan Aerospace Exploration Agency, Institute of Space and Astronautical Science, 3-1-1 Yoshino-dai, Chuo-ku, Sagamihara, Kanagawa 252-5210, Japan

⁴Department of Physics and Astronomy, University of Southampton, Highfield, SO17 1BJ Southampton, UK

*E-mail: morihana@u.phys.nagoya-u.ac.jp

Received ; Accepted

Abstract

Presence of the apparently extended hard (2–10 keV) X-ray emission along the Galactic plane has been known since the early 1980s. With a deep X-ray exposure using the Chandra X-ray Observatory of a slightly off-plane region in the Galactic bulge, most of the extended emission was resolved into faint discrete X-ray sources in the Fe K band (Revnivtsev et al. 2009). The major constituents of these sources have long been considered to be X-ray active stars and magnetic cataclysmic variables (CVs). However, recent works including our NIR imaging and spectroscopic studies (Morihana et al. 2013; Morihana et al. 2016) argue that other populations should be more dominant. To investigate this further, we conducted a much deeper NIR imaging observation at the center of the Chandra’s exposure field. We have used the MOIRCS on the Subaru telescope, reaching the limiting magnitude of ~ 18 mag in the J , H , and K_s bands in this crowded region, and identified $\sim 50\%$ of the X-ray sources with NIR candidate counterparts. We classified the X-ray sources into three groups (A, B, and C) based on their positions in the X-ray color-color diagram and characterized them based on the X-ray and NIR features. We argue that the major populations of the Group A and C sources are, respectively, CVs (binaries containing magnetic or non-magnetic white dwarfs with high accretion rates) and X-ray active stars. The major population of the Group B sources is presumably WD binaries with low mass accretion rates. The Fe K equivalent width in the composite X-ray spectrum of the Group B sources is the largest among the three and comparable to that of the Galactic bulge X-ray emission. This leads us to speculate that there are numerous WD binaries with low mass accretion rates, which are not recognized as CVs, but are the major contributor of the apparently extended X-ray emission.

Key words: Galaxy: stellar content — X-rays: stars — stars: cataclysmic variables — stars: late-type —

X-rays: diffuse background

1 Introduction

Presence of the apparently extended hard (≥ 2 keV) X-ray emission along the Galactic plane has been known since the early 1980s (e.g., Worrall et al. 1982). The emission has an integrated luminosity of $\sim 1 \times 10^{38}$ erg s $^{-1}$ in the 2–10 keV band (Koyama et al. 1986; Valinia & Marshall 1998) with a spectrum described by two-temperature thermal plasma ($k_B T \sim 1$ and 5–10 keV). A remarkable feature in the X-ray spectrum is the strong Fe K emission line complex (e.g., Koyama et al. 1996, Ebisawa et al. 2008, Yamauchi et al. 2009, Heard & Warwick 2013) comprised of neutral or low ionization state line at 6.4 keV (Fe I) and highly-ionized ion lines at 6.7 (Fe XXV) and 7.0 keV (Fe XXVI). In the most recent review (Koyama 2018), three distinct components of the Galactic diffuse emission with different scale heights are distinguished; the Galactic center X-ray emission, Galactic ridge X-ray emission (GRXE), and Galactic bulge X-ray emission (GBXE). We mainly focus on the GBXE in this paper, with some notes on the GRXE.

With the advent of the Chandra X-ray Observatory (Weisskopf et al. 2002), a large fraction of the GBXE and GRXE was resolved into faint discrete sources. For the GBXE, Revnivtsev et al. (2009) conducted a deep observation of a slightly off-plane region in the Galactic bulge ($l = 0.^{\circ}08, b = -1.^{\circ}42$; the Chandra bulge field or CBF, hereafter) and argued that $\sim 88\%$ of the GBXE around the Fe K band was resolved into faint X-ray point sources down to a flux of $\sim 10^{-16}$ erg cm $^{-2}$ s $^{-1}$ at the 2–10 keV band. For the GRXE, Ebisawa et al. (2001; 2005) conducted a deep observation on the Galactic plane ($l = 28.^{\circ}5, b = 0.^{\circ}0$; the Chandra plane field or CPF, hereafter) and discussed that there are two distinct classes of the point sources based on the X-ray spectral hardness.

Because of the similarities in the composite X-ray spectra, it is likely that the same X-ray point source populations contribute to the GBXE and GRXE with a different fraction. Then, what are the populations of these faint X-ray point sources? The most popular ideas are X-ray active stars and magnetic cataclysmic variables (CV) such as intermediate polars (IPs). The former contributes to the soft emission, while the latter does to the hard emission (Revnivtsev et al. 2009; 2011, Yuasa et al. 2012; Hong 2012). More recently, importance of other populations is being recognized. For example, Nobukawa et al. (2016); Yamauchi et al. (2016); Xu et al. (2016) discussed that non-magnetic CVs should be also a major population.

It should be noted that these results are based on X-ray data alone, in which photon statistics are generally too poor to constrain the nature of individual sources. Thus, follow-up observations in longer wavelengths are needed. Because of

the large interstellar absorption toward the GBXE and GRXE, near-infrared (NIR) observations are more suited than such optical observations that can access CVs only within ~ 2 kpc (Motch et al. 2010). In our previous work (Moriwana 2012), we conducted NIR imaging observations of the CBF using the Simultaneous Infrared Imager for Unbiased Survey (SIRIUS: Nagayama et al. 2003) on the InfraRed Survey Facility (IRSF) telescope in the South African Astronomical Observatory. With a limiting magnitude of 16 mag in the J , H , and K_s -band, we identified candidate NIR counterparts to $\sim 11\%$ of the X-ray point sources. Upon these NIR-identified X-ray sources, we further carried out NIR spectroscopic observations using the SofI (Moorwood et al. 1998) on the New Technology Telescope and the MOIRCS (Multi-Object InfraRed Camera and Spectrograph; Ichikawa et al. 2006; Suzuki et al. 2008) on the Subaru in the multi-object spectroscopy mode (Moriwana et al. 2016). In most soft X-ray sources, we found NIR spectra with absorption features, which represent X-ray active stars. In only a few hard X-ray sources, we found NIR spectra with H and He emission lines, which represent CVs. Unexpectedly, we found a dozen of hard X-ray sources exhibiting NIR spectra with absorption features. We argued that they are new populations different from X-ray active stars or CVs. In fact, the new population is the most dominant to account for the Fe K emission line of the GBXE (Moriwana et al. 2013; 2016). However, due to the shallow limiting magnitude, the NIR identification rate was low, which did not allow us to accumulate sufficient samples to characterize and unveil the nature of these populations.

Here, we present the results of the NIR imaging survey of the CBF using the 8.2 m Subaru telescope to achieve much deeper observation than our previous study using the 1.4 m IRSF telescope. The outline of this paper is as follows. We present the observation and data set in § 2 and data reduction, analysis, and grouping in § 3. In § 4, we characterize each group of the point sources based on their X-ray and NIR characteristics, and speculate of the nature of the major population for each group. The summary is given in § 5.

2 Observations

A deep JHK_s imaging observation of the CBF was carried out using the MOIRCS on the Subaru telescope. MOIRCS is equipped with two 2048×2048 HgCdTe HAWAII-2 arrays and covers a 4×7 arcmin 2 field of view with a pixel scale of $0''.117$ pixel $^{-1}$ in the imaging mode.

We focused on the center region in the CBF, in which the X-ray position determination accuracy is the best. Among 2002 X-

ray point sources detected down to $\sim 10^{-16}$ erg cm $^{-2}$ s $^{-1}$ (2–8 keV; Revnivtsev et al. 2009) in the CBF, ~ 540 sources are located within our MOIRCS field of view (Moriwana et al. 2013). Figure 1 shows the field layout of the MOIRCS observations. The observation was conducted on 2012 May 8 with a seeing of $0''.38$ – $0''.70$. We used the standard circular dithering pattern of the MOIRCS imaging mode (one center and eight surrounding pointing) with a dithering amplitude of $\sim 15''$. Each frame was exposed for 21 s (J and K_s) and 16 s (H) to avoid saturation of the detectors. The total exposure time was ~ 25 (J), ~ 30 (H), and ~ 25 minutes (K_s).

Because the observed field is very crowded, we could not estimate the sky background level from the same image. We thus retrieved the MOIRCS archive data of non-crowded regions with similar observation setup and as close in time with our observation for each band for assessing the sky level. They are tabulated in Table 1.

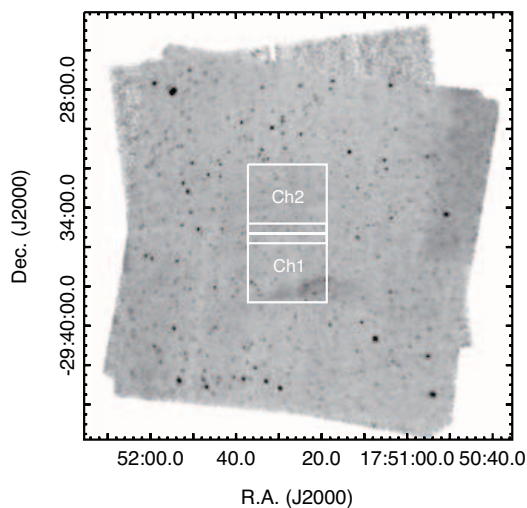


Fig. 1 Subaru/MOIRCS field layout superposed on the Chandra X-ray image in the CBF (Revnivtsev et al. 2009). The two white boxes represent the views of the two MOIRCS detector chips.

3 Data reduction & analysis

3.1 Reduction and source extraction

We used the MCSRED pipeline¹ developed for MOIRCS imaging data reduction based on the Infrared Reduction Analysis Facility (IRAF²). It executes dark frame subtraction, flat fielding, sky subtraction, correction for the optical distortion, measurements of positional offsets among dithered frames, and

¹ See <https://www.naoj.org/staff/ichi/MCSRED/mcsred.html> for detail.

² See <http://iraf.noao.edu/> for detail.

stacking the frames into one. The reduction was performed independently for each chip and band. They were combined into one image per band in the end.

We searched for sources in the J , H , and K_s bands separately using the SExtractor software (Bertin 1996). For the source extraction, we used a Gaussian smoothing filter with an FWHM of 3 pixels over 3×3 pixels. We detected 23,328, 23,267, and 21,903 sources in the J -, H -, and K_s -bands down to ~ 18 mag, respectively.

In order to calibrate the astrometry and photometry of the MOIRCS sources, we consulted to other NIR source catalogs in this region. In our previous work (Moriwana 2012), we presented the results of NIR imaging of the entire CBF using the 2MASS (Skrutskie et al. 2006) and the SIRIUS data. However, we could not utilize these catalogs because the most 2MASS and SIRIUS sources are saturated in the MOIRCS image. Just in between the dynamic range gap, there exist VISTA (the Visible and Infrared Survey Telescope for Astronomy) Variable in the Via Lactea (VVV) near-infrared imaging survey data release 2 (Minniti et al. 2018). The survey depth of the VISTA data is $K_s \sim 16.5$ mag (Saito et al. 2012), which is at least a magnitude deeper than those of 2MASS and SIRIUS.

We cross-correlated the MOIRCS and VVV sources and corrected the astrometry and photometry of the MOIRCS sources compared with the VVV sources. In figure 2, we compare VISTA and MOIRCS positional differences after the astrometric correction. The standard deviation of the systematic displacement between the VISTA and MOIRCS sources is $0''.078$ in R. A. and $0''.081$ in Dec., which are smaller than the pixel scale of MOIRCS ($0''.117$). After the correction of the MOIRCS positions to match with those of VVV, the residual offset is $< 0''.002$ in both R. A. and Dec. directions in all bands. In figure 3, we show correlations between VISTA and MOIRCS JHK_s magnitudes after the photometric correction. MOIRCS magnitudes are fainter than those of VISTA for the sources brighter than 13.5 mag, which is due to the saturation in MOIRCS. In the photometric calibration, therefore, we used only the sources in the magnitude ranges of 13.5–16.5 mag (J), 13.5–16.5 mag (H), and 13.5–16.5 mag (K_s).

To estimate the completeness of our data, we embedded 200 artificial objects in the MOIRCS image and attempted detecting them using the same source extraction algorithm. Here, we used the mkobject task of IRAF to embed 200 artificial sources in the magnitude ranges from 14.0 to 18.0 mag with a 0.5 mag step. We derived the detection rates for each range using the same detection algorithm. We regarded as detection if the embedded sources were detected at the same position with the same magnitude range as the input values within a margin. We estimated the 90% and 50% completeness limits for each band as follows; 17.0 mag and 18.0 mag in J band, 16.5 mag and 17.5 mag in H band, and 16.5 mag and 17.5 mag in K_s band.

Table 1 Subaru observation log.

Object	R. A. (J2000)	Dec. (J2000)	Exp. time (min)	Obs. date	Airmass
Chandra Bulge Field (CBF)	17:51:27.86	-29:35:31.40	25 (J , K_s), 30 (H)	2012-05-08	1.535–1.762
QUARET (J -band sky)	18:36:10.28	-07:07:10.29	49	2012-06-11	1.236–1.551
G24.47+0.49 (H -band sky)	18:34:06.34	-07:19:39.82	40	2012-06-11	1.125–1.134
SSA22 (K_s -band sky)	22:17:22.58	+00:17:55.15	8	2012-06-11	1.061

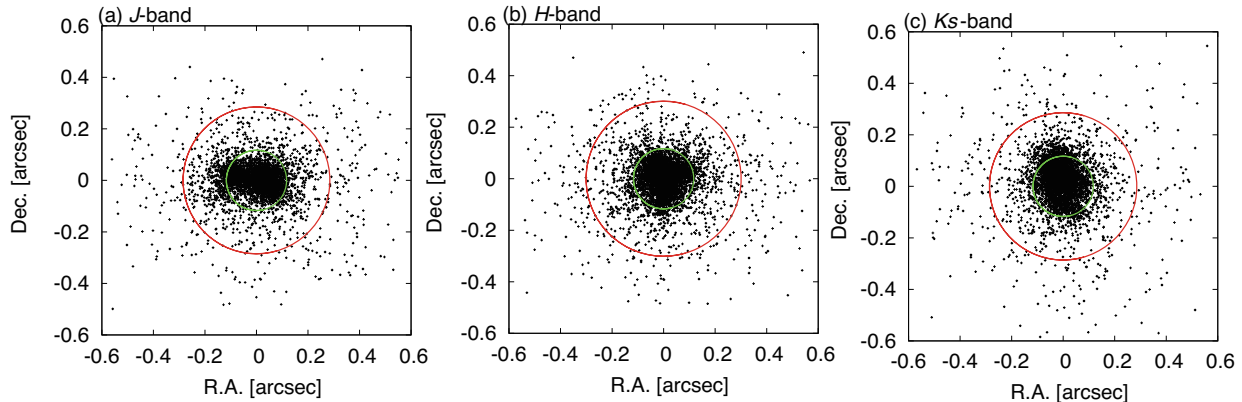


Fig. 2 Displacements of MOIRCS from VISTA sources after the astrometric correction separately for the J , H , and K_s -band. The red and green circles show 3σ radius of the displacement and 1 pixel ($0''.117$) radius of MOIRCS, respectively.

3.2 NIR identification of X-ray sources

We look for candidate NIR counterparts to the Chandra X-ray sources. For the NIR sources brighter than 13.5 (J), 14.0 (H), and 14.0 (K_s) magnitudes, we use the result of our previous work (Morihana 2012). In the present work, we extend the identification to fainter NIR magnitudes using the MOIRCS data. The search radius was set as $0''.5$, which is comparable to the quadrature sum ($0''.62$) of the relative and absolute astrometric errors of X-ray and NIR sources. The following known terms were added in quadrature: (a) the error in the absolute astrometry of Chandra ($0''.58$; ACIS-I,³), (b) the relative astrometry errors of Chandra sources (values in table 3, we adopted a typical value of $0''.2$), (c) the error in the absolute astrometry of VISTA ($0''.07$, Saito et al. 2012), and (d) the relative astrometry errors of the NIR sources ($0''.112$; figure 2). First, we searched for the nearest NIR source for each X-ray source and also the nearest X-ray source for each NIR source. We then regarded them candidate NIR counterparts if a NIR and X-ray source pair is closest to each other. An example is shown in figure 4. The resultant offset between the X-ray and NIR sources is $0''.085$, which is sufficiently small in comparison with the search radius. As a result, we identified MOIRCS counterparts to $\sim 40\%$ of the X-ray sources. This is significantly larger than our previous result of $\sim 11\%$ using 2MASS and SIRIUS surveys (Morihana 2012). The statistics are shown in table 2 and the counterpart table is shown in table 3. Both tables include the results of Morihana

(2012) and the present study. All together, we identified $\sim 50\%$ of the X-ray sources with candidate NIR counterparts.

Table 2 Summary of NIR identification.

	Num. of sources			NIR ID Rate		
	J	H	K_s	J	H	K_s
X-ray Point Sources*	533	539	530	–	–	–
2MASS & SIRIUS IDed [†]	49	46	44	9%	9%	8%
MOIRCS IDed	206	194	205	39%	36%	39%
2MASS+SIRIUS+MOIRCS IDed	255	240	249	48%	45%	47%

*Number of the X-ray point sources detected by Morihana et al. (2013) within the image of each band. [†]Number of the X-ray point sources with candidate 2MASS or SIRIUS counterparts (Morihana 2012).

In the crowded regions such as the one presented here, false positive counterparts (unrelated pairs identified as counterparts) are unavoidable. We assessed the number of the false positive counterparts (N_{FP}) by

$$N_{\text{FP}} = N_X \pi r^2 \Sigma, \quad (1)$$

where N_X is the number of the X-ray sources, $r = 0''.5$ is the counterpart search radius, and Σ is the surface number density of NIR sources, which varies as a function of the magnitude in each band (table 4). The false positive rate increases as the magnitude increases in general. As shown in table 4, the false positive is estimated to be more than a half of the candidates in the range of 17–18 mag in H - and K_s -bands. Thus, we discard the candidates with H - or K_s -band magnitudes larger than 17 mag in the following analysis. Except for these, the average

³ See <https://cxc.harvard.edu/cal/ASPECT/celmon/>

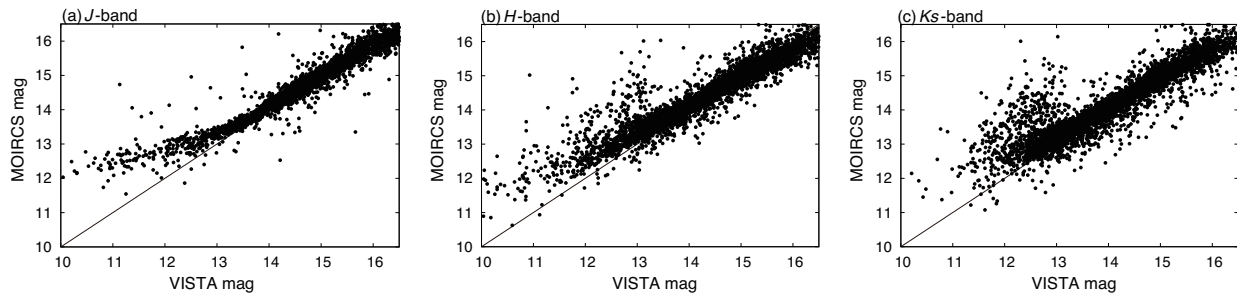
Fig. 3 Comparison of MOIRCS and VISTA photometry separately for the J , H , and K_s -band.

Table 3 NIR identified X-ray source catalog.

Source		Position				Characteristics			Photometry					
Number	CXOU J	R. A. (X)	Dec. (X)	R. A. (NIR)	Dec. (NIR)	Err	Phot F_x (0.5–8 keV)	Phot F_x (2–8 keV)	J	J_{err}	H	H_{err}	K_s	$K_{s, err}$
#	(2)	(deg)	(deg)	(deg)	(deg)	($''$)	($\text{ergs cm}^{-2} \text{s}^{-1}$)	($\text{ergs cm}^{-2} \text{s}^{-1}$)	(mag)	(mag)	(mag)	(mag)	(mag)	(mag)
(1)	(2)	(3)	(4)	(5)	(6)	(7)	(8)	(9)	(10)	(11)	(12)	(13)	(14)	(15)
1000	175128.13–293703.7	267.867210	-29.61772	267.86730	-29.61760	0.1	2.9×10^{-16}	6.8×10^{-17}	11.26	0.01	10.95	0.01	10.92	0.01
1004	175128.20–293347.0	267.867530	-29.56306	267.86750	-29.56310	0.1	8.0×10^{-16}	5.4×10^{-16}	10.86	0.01	0.00	0.00	0.00	0.00
1006	175128.25–293248.3	267.867730	-29.54677	267.86768	-29.54680	0.2	1.5×10^{-16}	1.3×10^{-16}	17.97	0.12	0.00	0.00	16.63	0.10
1010	175128.35–293621.5	267.868140	-29.60599	267.86810	-29.60610	0.1	1.8×10^{-16}	1.2×10^{-16}	15.12	0.10	14.20	0.12	14.20	0.14
1011	175128.36–293714.7	267.868170	-29.62076	267.86811	-29.62069	0.1	1.5×10^{-16}	1.2×10^{-16}	14.96	0.01	14.30	0.01	14.13	0.01
1013	175128.38–293438.2	267.868290	-29.57729	267.86826	-29.57723	0.1	1.2×10^{-16}	6.4×10^{-17}	16.65	0.04	16.04	0.05	15.82	0.04
1014	175128.39–293215.4	267.868330	-29.53762	267.86837	-29.53753	0.2	2.5×10^{-16}	2.4×10^{-16}	17.53	0.09	16.63	0.08	15.97	0.07
1019	175128.48–293625.0	267.868680	-29.60696	267.86860	-29.60690	0.1	1.4×10^{-16}	4.7×10^{-18}	13.71	0.03	12.66	0.02	12.32	0.02
1020	175128.52–293328.7	267.868870	-29.55798	267.86888	-29.55798	0.0	1.0×10^{-15}	4.7×10^{-16}	15.61	0.03	14.99	0.03	14.71	0.02
1022	175128.57–293220.9	267.869060	-29.53916	267.86892	-29.53925	0.2	1.6×10^{-16}	1.1×10^{-16}	15.34	0.01	0.00	0.00	14.71	0.02

Col. (1): X-ray catalog source number in Morihana et al. (2013), sorted by R.A. Col. (2): IAU designation. Col. (3)–(6) : R.A. and Dec. in the equinox J2000.0 by X-ray and NIR. Col. (7): X-ray position error (1σ). Col. (8), (9) : Photometric flux in the total (0.5–8.0 keV) and the hard (2.0–8.0 keV) band. The photometric flux is defined as count rate multiplied by the median energy divided by the average effective area (Tsujiimoto et al. 2005; Morihana et al. 2013). Col. (10)–(15): NIR magnitude and error. (A portion of the catalog is shown here for guidance regarding its form and content. The full version is shown in a machine-readable form in the online journal.)

false positive rate is 25%. To validate the false positive number estimates, we did the following exercise. We artificially displaced the relative positions of the X-ray and NIR sources in the R.A. or Declination directions by $\pm 1-10''$ and identified the counterpart pairs using the same method. The resultant number of counterpart pairs at large displacements are found consistent with the number of false positive estimates in table 4.

We also assessed the number of false negatives (N_{FN} ; related pairs not identified as counterparts due to the separation of X-ray and NIR sources are larger than search radius) by

$$N_{FN} = N_X f e^{-\left(\frac{r}{\sigma}\right)^2}, \quad (2)$$

where f is the ratio of the X-ray sources with NIR counterparts (to all X-ray sources and $\sigma = 0.''16$ is the quadrature sum of the typical X-ray (table 3) and NIR (figure 2) positional uncertainty. We found that the false negative is negligible (less than 1% of the number of the false positive) in all the magnitude ranges.

3.3 Grouping

For all the X-ray sources with NIR counterparts, we classify them into groups based on their X-ray colors. Most of the X-ray sources have poor photon statistics, thus we used the method

based on the color quantiles developed by Hong et al. (2004), which was also adopted in our previous work (Morihana et al. 2013). Here, the quantile E_x (keV) is the energy below which $x\%$ of X-ray photons reside in the energy-sorted list of photons. The quantile is normalized as

$$Q_x = \frac{E_x - E_{\min}}{E_{\max} - E_{\min}}, \quad (3)$$

in which E_{\min} and E_{\max} are the lower and upper bounds of the energy (0.5 and 8 keV), respectively. We used Q_{25} , Q_{50} , and Q_{75} , and defined two metrics as $q_1 = \log_{10} Q_{50} / (1 - Q_{50})$ and $q_2 = 3Q_{25} / Q_{75}$. Here, the metric q_1 reflects the degree of photon spectrum being biased toward the harder (q_1 is large) or softer (q_1 is small) end, and the metric q_2 reflects the degree of photon spectrum being less (q_2 is large) or more (q_2 is small) concentrated around the peak. The metric q_1 is a proxy to the more often-used hardness ratio or the median energy. We plotted all the X-ray sources detected in the CBF in the q_1 - q_2 plane (figure 5). The distribution is characterized by a concentration at $q_1 \sim -0.7$ and $q_2 \sim 0.8$ and two branches extending upward and rightward. Following our previous work (Morihana et al. 2013), we used the k -means clustering algorithm method (Macqueen 1967), which defines groups to minimize the distance from each source to the centroid of each group. As a

Table 4 Estimates of false positive detections.

Range (mag)	$N_{X, \text{MOIRCS}}^*$			Σ^\dagger (arcsec $^{-2}$)			N_{FP}^\ddagger		
	<i>J</i>	<i>H</i>	<i>K_s</i>	<i>J</i>	<i>H</i>	<i>K_s</i>	<i>J</i>	<i>H</i>	<i>K_s</i>
14–15	29	48	59	0.022	0.024	0.026	9.2 (32%)	10.2 (21%)	10.8 (18%)
15–16	61	56	58	0.023	0.031	0.034	9.6 (16%)	13.1 (23%)	14.1 (24%)
16–17	58	63	62	0.038	0.048	0.040	15.9 (27%)	20.3 (32%)	16.6 (27%)
17–18	60	21	12	0.049	0.033	0.019	20.5 (34%)	14.0 (67%)	7.9(66%)

* Number of MOIRCS-identified X-ray sources. † Surface number density of MOIRCS sources. ‡ Estimated number of false positive detections and false positive rate. The number in parentheses represents the false positive rate.

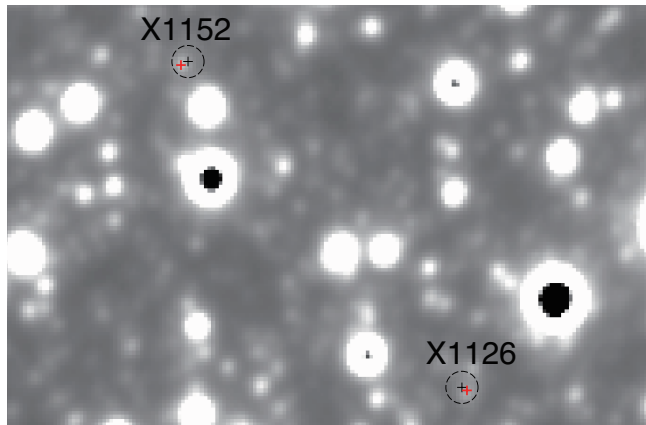


Fig. 4 Examples of the new MOIRCS identification of the X-ray sources. The X-ray source positions (source names starting with X in Morihana et al. 2013) are shown with black crosses and their typical positional uncertainty ($0.5''$) with broken circles on the MOIRCS K_s -band image. Their NIR counterpart candidates are shown with red crosses. K_s -band magnitude of the two sources are 16.88 mag (X1126) and 16.21 mag (X1152), respectively.

result, we qualitatively classified the sources into three groups A, B, and C. We estimate the false positive rate of each group to be 41% (A), 34% (B), and 25% (C) from the expected false positive numbers derived from large search radii.

4 Discussion

We now discuss nature of the faint X-ray sources based on the grouping defined in §3.3. Given the rate of false positive NIR counterparts (§ 3.2), we limit ourselves to discuss the overall characteristics of groups and not individual sources. In § 4.1, we derive general characteristics of each group as follows; NIR and optical identification rates (§ 4.1.1), composite X-ray spectrum (§ 4.1.2), X-ray variability (§ 4.1.3), X-ray to NIR flux ratio (§ 4.1.4), and the distance and X-ray luminosity based on the parallax measurements by Gaia (§ 4.1.5). In § 4.2, we discuss the likely nature for the primary constituent of each group. In

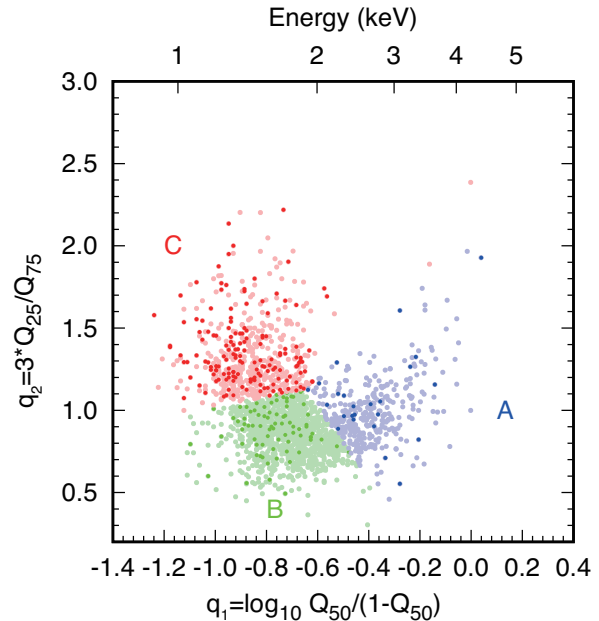


Fig. 5 Quantile distribution of all the X-ray sources detected in the CBF (pale colors; Morihana et al. 2013) and those with NIR counterparts (dark colors). Different colors are used for the three groups. The median energy equivalent to each q_1 is given in the upper horizontal axis.

§ 4.3, we discuss the populations that mostly contribute to the GBXE.

4.1 Characteristics of the X-ray sources

4.1.1 NIR and optical identification rates

Table 5 shows a summary of our NIR identification rate of the X-ray sources for each group. In addition, we retrieved the Gaia data release 2 (Prusti et al. 2016). We searched for Gaia G -band ($0.33\text{--}1.0\ \mu\text{m}$) counterparts of all the X-ray sources using the same method as in § 3.2. With a search radius of $0''.5$, we identified the Gaia counterparts to 109 X-ray sources down to 19.5 mag. Among the 109 sources, six of them were identified using optical images taken with the Hubble Space Telescope (tables 3–5 in van den Berg et al. 2009). The false positive rate

is estimated to be $\sim 17\%$. About a half of them have a distance estimate based on the parallax. The optical identification rate is also given in table 5.

Table 5 Summary of identification in each group.

Group	Num. of X-ray sources	Rate _{NIR} [*]	Rate _{opt} [†]	Rate _{dist} [‡]
A	89	27% (24)	7% (6)	2% (2)
B	189	42% (80)	12% (23)	8% (15)
C	270	59% (160)	30% (80)	16% (44)
Total	548	48% (264)	20% (109)	11% (61)

^{*}NIR Identification rate. The number in parentheses indicates the number of sources. [†]Optical identification rate. [‡]Optical identification rate with a distance estimate by Gaia.

4.1.2 X-ray composite spectra

We made a composite 0.5–8 keV spectrum of all the X-ray sources in each group. We used the `combine_spectra` tool in the CIAO package, which makes averaged combined background-subtracted spectra as well as count-weighted telescope and instrument response functions. We binned the spectra to have more than 20 counts per bin and fitted them based on the χ^2 statistics.

For the spectral models, we used optically-thin thermal plasma model (Smith et al. 2001) or a power-law model attenuated by the interstellar photo-electric absorption model (Wilms et al. 2000). Free parameters for the thermal model are the plasma temperature ($k_B T$), the metal abundance (Z), and the flux (F_X) in the 0.5–8.0 keV band. Those for the power-law model are the photon index (Γ) and the flux (F_X). Free parameter for the absorption model is the absorption column density (N_H). We regarded the fitting to be unsuccessful if the reduced χ^2 was larger than 1.5 or the best-fit parameters were unphysical; $\Gamma > 3$ in the power-law fitting or $k_B T > 15$ keV in the thermal fitting.

We started fitting the spectra with a single thermal plasma or a single power-law model. The fitting was not successful for all the groups. We then added a second continuum component and fitted the spectra with two thermal components of different temperatures or a one-temperature thermal plus a power-law component. The fitting was successful for all the groups. When both models yielded successful fitting, we adopted the one with the smaller χ^2 value. The result is given in figure 6 for the spectra and best-fit models and in table 6 for the best-fit parameters.

The composite spectra show signatures of the Fe K line feature. We derived their equivalent width (EW) by locally fitting the spectra in the 4–8 keV range with a power-law and a Gaussian line. With the energy resolution of Chandra, we cannot separate the 6.4, 6.7, and 7.0 keV lines, thus we treated them as a single emission line. The free parameters are the photon index and flux of the power-law and the line center and the normalization of the Gaussian component. The line width was

fixed to 0.01 keV. We tested the necessity of the Gaussian component using the F-test and found that it was indeed required for Group A and B spectra with significances of 87.5% and 91.6% retrospectively. On the other hand, the significance of F-test of Group C is low, indicating that it does not require a significant Gaussian component. This can be attributed to the lack of the photon statistics in Group C. The result is shown in table 7.

We further obtained the X-ray surface brightness 2.7×10^{-11} erg cm⁻² s⁻¹ deg⁻² in 2–8 keV by averaging all the X-ray point sources identified in NIR. From Iso et al. (2012), the entire X-ray surface brightness of the GBXE in the same band is 1.01×10^{-10} erg cm⁻² s⁻¹ deg⁻². As a result, we estimate that X-ray surface brightness from the X-ray point sources with NIR counterpart candidates in this and our previous studies account for $\sim 26\%$ of the entire X-ray surface brightness of the GBXE.

4.1.3 X-ray variability

We investigated temporal behavior of the X-ray sources with NIR counterparts. For all the X-ray sources with NIR counterparts, we applied the Kolmogorov-Smirnov (KS) test against the null hypothesis that the X-ray light curves are constant. We consider that the sources with the null hypothesis probability (P_{K-S}) of $< 5 \times 10^{-3}$ as “definitely variable” and those with $5 \times 10^{-3} < P_{K-S} < 5 \times 10^{-2}$ as “possibly variable”. As a result, 11 sources are definitely variable and 19 are possibly variable (table 8). Almost all the variable sources belong to Group B or C, and more than a half belong to Group C.

4.1.4 X-ray to NIR flux ratio

We investigated ratio of the X-ray flux to the NIR flux. The ratio is expected to be relatively high for the binaries containing compact objects and low for stellar sources. We employed the photometric X-ray flux at 2–8 keV (table 3 column 9) estimated from the count rates and the median energies (Moriwana et al. 2013). Figure 7 top panel shows the ratio between the hard (2–8 keV) X-ray ($F_{X,h}$) against NIR flux (F_{NIR}) for all the X-ray sources with NIR counterparts. F_{NIR} is defined as $F_{0\lambda} d\lambda 10^{-0.4m}$, where $F_{0\lambda}$, $d\lambda$, and m are the flux at 0 mag for each band, the band width, and the Vega magnitude, respectively. The logarithm of the ratio ($\log F_{X,h}/F_{NIR}$) shows different distributions among the three groups, which are more influenced by the differences of $F_{X,h}$ than that of F_{NIR} . This is depicted in figure 7 bottom panels, which show the histograms of $F_{X,h}/F_{NIR}$ values. For example, in the $\log F_{X,h}/F_{Ks}$ plot (figure 7c), sources span in the range of -3 to -1 (Group A), -4 to -2 (Group B), and from -6 to -2 (Group C). We also plotted the flux ratios of several representative sources with known nature that are for candidates of the X-ray point sources constituting the GBXE.

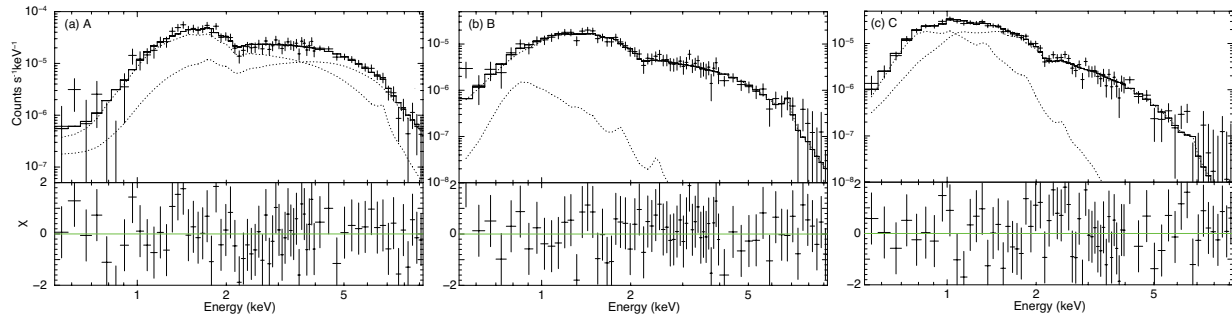


Fig. 6 Composite X-ray spectra and the best-fit models of the three groups (A, B, and C). Grouped data (pluses) and the best-fit model convolved with the instrumental response (solid histograms) are shown in the upper panel, while the residuals to the fit are shown in the lower panel. The best-fit parameters are given in table 6.

Table 6 Best-fit parameters for the composite spectra of the three groups.

Group	N_{H}^* (10^{22} cm^{-2})	$k_{\text{B}}T_1^*$ (keV)	$k_{\text{B}}T_2^*$ (keV)	Z^*	Γ^*	$\chi^2/\text{d.o.f}$
A	$0.92^{+0.14}_{-0.32}$	$4.6^{+7.7}_{-1.9}$	–	$0.21^{+0.50}_{-0.18}$	$0.25^{+0.60}_{-0.25}$	55.35/70
B	$0.38^{+0.34}_{-0.12}$	$0.7^{+0.3}_{-0.5}$	$6.3^{+2.0}_{-1.2}$	$1.01^{+1.16}_{-0.87}$	–	41.14/70
C	$0.40^{+0.19}_{-0.18}$	$0.6^{+0.3}_{-0.1}$	$2.0^{+0.4}_{-0.2}$	$0.22^{+0.18}_{-0.11}$	–	61.12/70

* Uncertainties represent 90% confidence intervals.

Table 7 Best-fit parameters for Fe K line fitting.

Group	Energy center* (keV)	EW* (eV)
A	$6.67^{+0.10}_{-0.11}$	162^{+18}_{-26}
B	$6.76^{+0.13}_{-0.44}$	488^{+50}_{-91}
C	6.70 (fix)	3 (upper limit)

* Uncertainties represent 90% confidence intervals.

Table 8 Time variable sources.

Group	Definitely*	Possibly*
A	0	1
B	5	6
C	6	12
Sum	11	19

* Based on the null hypothesis probability of the K-S test: $< 5 \times 10^{-3}$ (definitely variable) or $5 \times 10^{-3} - 5 \times 10^{-2}$ (possibly variable).

4.1.5 Distance and X-ray luminosity

Almost all the previous works discussing X-ray point sources constituting the GBXE and GRXE were based on the flux without knowing the distance. Now, we have identified 109 Gaia counterparts (§ 4.1.1). Among them, 61 sources have parallax measurements (Bailer-Jones et al. 2018). The breakdown is that 2, 15, and 44 sources belong to the Group A, B, and C, respectively (table 5). We derived their distance and X-ray luminosity (L_{X}) in the 2–8 keV band without correcting the interstellar absorption. The distance and luminosity distributions are shown in figure 8. We found that most (if not all, given the large distance errors) X-ray sources with Gaia counterparts are

within 4 kpc thus are foreground objects to the GBXE. Here, one should keep in mind that the false positive rates among the Gaia matches are from 7% (Group A) to 30% (Group C). The average X-ray luminosity of each group is $\sim 10^{30.4^{+1.2}_{-0.5}} \text{ erg s}^{-1}$ (Group A), $\sim 10^{29.6^{+0.3}_{-0.8}} \text{ erg s}^{-1}$ (Group B), and $\sim 10^{29.2^{+0.4}_{-0.4}} \text{ erg s}^{-1}$ (Group C).

4.1.6 NIR spectroscopy results

In our previous work (Morihana et al. 2016), we carried out NIR spectroscopy for 23 of the present sources in the CBF and 40 sources in the CPF. To compensate for the paucity of the statistics in the CBF alone, we also refer to the result in the CPF here. To facilitate the comparison between the two fields, we constructed the q_1 - q_2 diagram for the CPF (figure 9) and classified the NIR-identified X-ray sources into Groups A–C using the same algorithm described in § 3.3. Due to the difference of the extinction toward CBF and CPF, the scatter of the data is different, but the overall trend is similar to each other.

Three distinctive types were found based on the combination of X-ray spectral hardness and NIR line features; hard X-ray sources with NIR emission features of H I and He II (H+emi), hard X-ray sources with NIR absorption features (H+abs), and soft X-ray sources with NIR absorption features (S+abs). Here, the X-ray spectral hardness is defined by hardness ratio as $(H - S)/(H + S)$ where H and S are the normalized count rates in the hard (2–8 keV) band and soft (0.5–2 keV) band. We show their distribution in the q_1 - q_2 diagram in figure 9 and statistics in table 9. It should be noted that the NIR features, which are

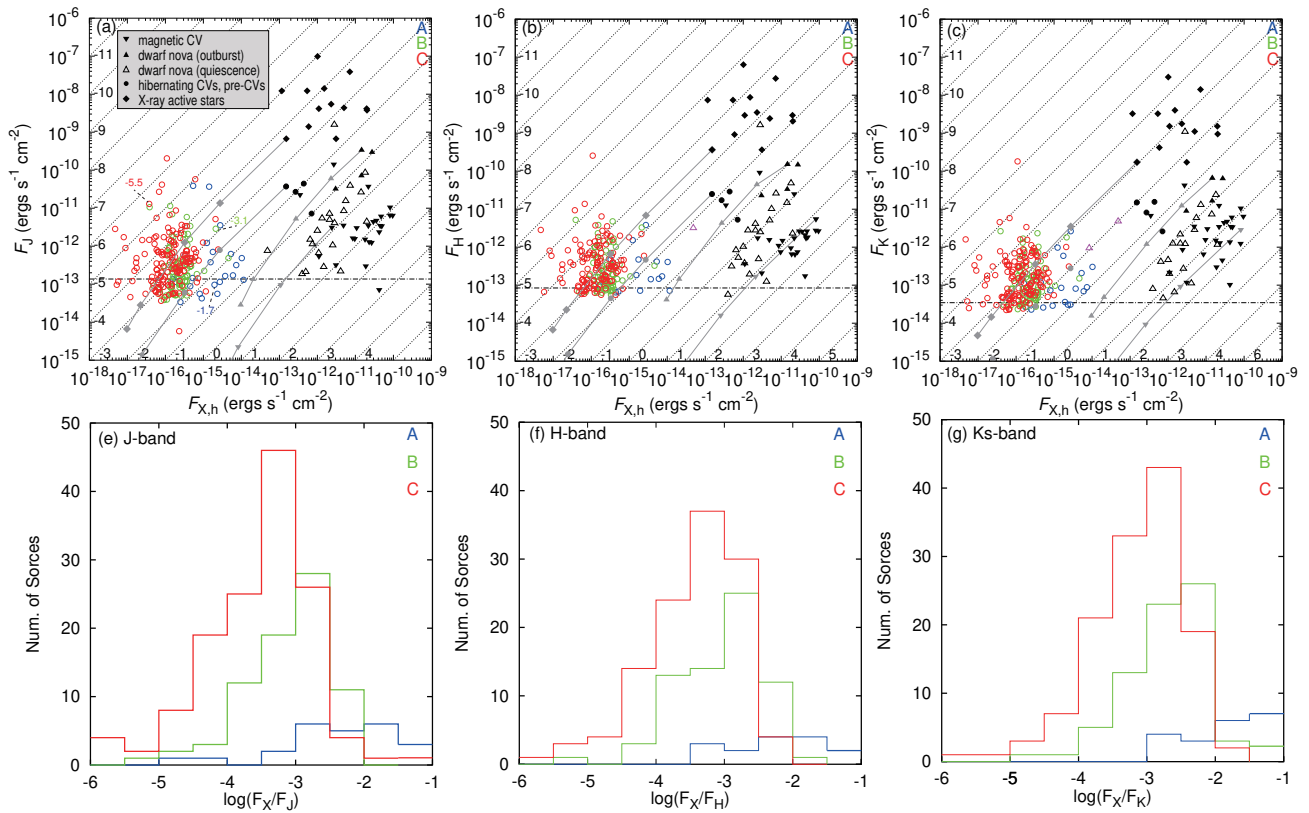


Fig. 7 (Top) Flux ratio between the hard (2–8 keV) X-ray and (a) *J*-band, (b) *H*-band, or (c) *K_s*-band flux of the X-ray sources with NIR counterparts. The dotted lines indicate the iso-flux-ratio with its logarithmic values given along the *x* and *y* axes. Different colors are assigned based on the grouping in § 3.3. The purple triangle shows hard X-ray sources with NIR emission features (§ 4.1.6). The horizontal dashed-line in the panels of the upper figures indicate the 90% completeness limit of each band. Representative sources of the following categories are shown for comparison in different symbols in black as in the legend in (a); (i) magnetic CVs (polars; Ezuka & Ishida 1999; Mukai 2017; Xu et al. 2016 and intermediate polars; Ezuka & Ishida 1999; Mukai 2017; Xu et al. 2016), (ii) dwarf novae (Baskill et al. 2005; Wada et al. 2017; Ebisawa et al. 2005; Xu et al. 2016; Wada et al. 2017), (iii) hibernating CVs, pre-CVs (Matranga et al. 2012; Schwope et al. 2014), (iv) active stars (during flares; Pandey & Singh 2008; Pandey & Singh 2012; Tsuboi et al. 2016 and in quiescence; Pandey & Singh 2008). For several sources, we also showed the expected trajectories when the distance (and proportionally the extinction column proportional to the distance) increases as $N_{\text{H}} = 1 \times 10^{21}$ (~ 350 pc), 3×10^{21} (~ 1 kpc), 1×10^{22} (~ 3 kpc), 1.5×10^{22} (~ 5 kpc) with the solid lines from upper-right to lower-left. The relation between the column density and the distance is based on the typical hydrogen column density $\sim 1 \text{ cm}^{-3}$ of the interstellar medium. We used the *wabs* model (Morrison & McCammon 1983) with the abundance table (Anders & Grevesse 1989) for the extinction calculation. (Bottom) distribution of the F_X/F_{NIR} values in the (d) *J*-, (e) *H*-, and (f) *K_s*-bands.

unrelated to q_1 or q_2 by definition, are distributed in a biased manner in the diagram. For example, the hard X-ray sources with NIR emission features (H+emi, only found in CPF) belong to Group A. Group C sources only consist of the soft X-ray sources with NIR absorption features (S+abs).

Table 9 Results of NIR spectroscopy.

Group*	CBF [†]	CPF [†]
A	H+abs (3)	H+emi (2), H+abs (5)
B	H+abs (7), S+abs (4)	H+abs (15), S+abs (4)
C	S+abs (9)	S+abs (14)

* Groups defined in the X-ray color-color diagram (figure 5). † Number of sources in the parentheses based on the X-ray spectral hardness (“S”oft or “H”ard) + NIR “emi”ssion or “abs”orption features.

4.2 Major populations

Based on the characterizations in various aspects shown in § 4.1, we summarize distinctive characteristics of the sources in simplicity order of the features— Group C, A, and B.

4.2.1 Group C

The first is the Group C sources, which have the following properties distinctive from the others:

- (1) The composite X-ray spectrum is represented by a two-temperature thermal plasma model with temperatures of $k_B T \sim 0.6$ and 2.0 keV (table 6). Unlike the other groups, Fe K line was not observed significantly (table 7).
- (2) The fraction of time-variable sources is the largest (table 8).
- (3) The ratio of X-ray to NIR flux is the lowest in the range of 10^{-6} to 10^{-2} (figure 7).
- (4) The fraction of optically-identified sources is the largest (table 5). Most sources are located within 4 kpc (figure 8). The average X-ray luminosity is the lowest, $1.57 \times 10^{29} \text{ erg s}^{-1}$

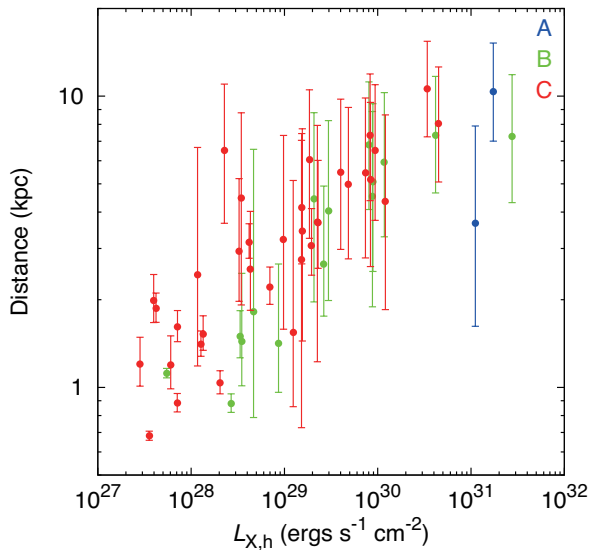


Fig. 8 Scatter plot of the distance by Gaia (Bailer-Jones et al. 2018) and the 2–8 keV X-ray luminosity for the sources with distance estimates.

in the 2–8 keV band.

- (5) All the Group C sources studied in the NIR spectroscopy exhibit absorption features typical of late-type stars (Morihana et al. 2016).

These characteristics are most consistent as the major population of the Group C sources being the X-ray active stars. The plasma temperatures and X-ray luminosity are consistent with the values typically seen in X-ray active stars such as RS CVn systems (Dempsey et al. 1993; Güdel et al. 1999; Covino et al. 2000; Pandey & Singh 2012). The ratio of X-ray to NIR flux that mainly driven by the differences in $F_{X,h}$ is also consistent with those of representative sources (figure 7). The high fraction of the X-ray variable sources is understood, because the X-ray active stars show occasional flare-like activities. Average X-ray luminosity of the optically-identified sources is consistent with that of the typical value (10^{27} – 10^{30} erg s $^{-1}$; Schmitt et al. 1990) of X-ray active stars. From the above characteristics, we argue that the major population of the Group C sources is X-ray active stars.

4.2.2 Group A

We next discuss the Group A sources, which have the following characteristics:

- (1) The composite X-ray spectrum is described by the combination of a thermal plasma model with $k_B T \sim 4.6$ keV and a power-law model with $\Gamma = 0.25$ (table 6). The Fe K line was detected with the center at 6.7 keV and the EW of 162 eV (table 7).
- (2) None but one source shows X-ray variability (table 8).

- (3) The ratio of X-ray to NIR flux is the largest with 10^{-3} to 10^{-1} (figure 7).
- (4) The fraction of optically-identified sources is the smallest (table 5). The average X-ray luminosity of the optically-identified sources is $\sim 10^{30}$ erg s $^{-1}$ in the 2–8 keV band, the largest among the three groups.
- (5) All the hard X-ray sources with NIR emission features belong to Group A. Group A sources also include hard X-ray sources with NIR absorption features (table 9).

We interpret these features that the Group A sources are a mixture of the magnetic and non-magnetic CVs. The ratio of the X-ray to NIR flux (figure 7) is consistent with those of representative magnetic CVs and dwarf novae. They are time variable from their names, but the occurrence of such variability is less frequent than flares in X-ray active stars and its duration is long, hence a fraction of the X-ray variable sources is considered small. All the sources with the NIR emission line features of H I and He II belong to this group, which is consistent with the idea that the Group A sources are those with prominent accretion disks. Those without the emission features are presumably sources with an accretion rate that is too small to exhibit prominent emission lines over the stellar photospheric absorption features.

The typical EW of the Fe K lines (6.4, 6.7, and 7.0 keV combined) is ~ 350 eV for magnetic CVs and ~ 700 eV for non-magnetic CVs (Koyama 2018). The EW of the composite spectrum of the Group A sources is smaller. Therefore, contribution of the non-magnetic CVs is considered sub-dominant.

4.2.3 Group B

Finally, we discuss Group B sources with the following characteristics:

- (1) Some sources exhibit X-ray variability (table 8).
- (2) Ratio of the X-ray to NIR flux is in the range of 10^{-4} to 10^{-2} , between Group A and C (figure 7).
- (3) Fraction of the optically-identified sources is the second largest next to Group C (table 5). The average X-ray luminosity is 3.7×10^{29} erg s $^{-1}$ in the 2–8 keV band, the second largest next to Group A.
- (4) All the sources with the NIR spectra exhibited absorption features typical of the late-type stars (Morihana et al. 2016).
- (5) The composite X-ray spectrum is described by a two-temperature thermal plasma model with temperatures of $k_B T \sim 0.7$ and 6.3 keV (table 6). The Fe K line is the strongest with an EW of ~ 500 eV (table 7).

Most of these characteristics are in between Group A and C as expected from the definition in figure 5. However, we do not consider that the Group B sources are a mere mixture of the major populations of the Group A and C sources. This is because the Fe K line EW of the Group B average X-ray spectrum

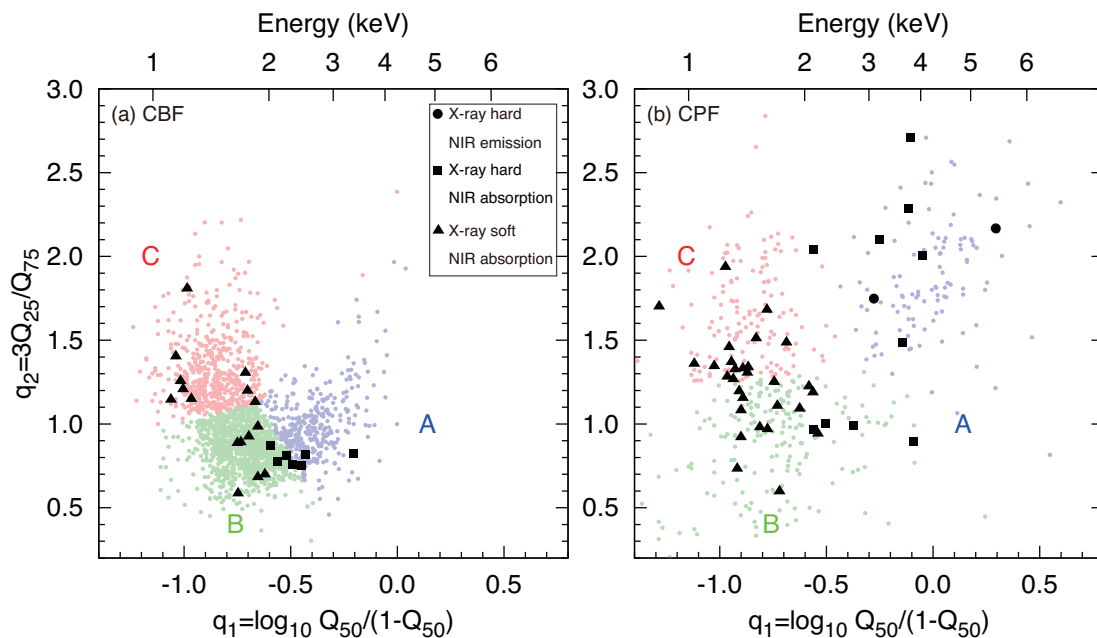


Fig. 9 Quantile distribution of all the X-ray sources (pale colors) and those with NIR spectroscopic results in the CBF (left) and the CPF (right). Black filled circles, squares, and triangles respectively indicate X-ray hard sources with NIR emission features (H+emi in table 9), X-ray hard sources with NIR absorption features (H+abs), and X-ray soft sources with NIR absorption sources (S+abs). The typical error of q_1 and q_2 are 0.02 and 0.06, respectively, for a source with average 40 counts. The minimum and maximum numbers of the counts for the X-ray sources with NIR spectra are 12 counts and 222 counts, respectively.

is the largest of the three groups, which cannot be explained by the combination of Group A and C. We speculate that, unlike Group A, non-magnetic CVs are dominant in Group B.

However, the Group B sources also have the characteristics that cannot be explained by *known* non-magnetic CVs (or, sources identified as dwarf novae) alone. The ratios of the X-ray to NIR fluxes and the typical X-ray luminosities are both smaller than those of dwarf novae (figure 7). NIR spectra of dwarf novae often exhibit H I emission lines (Dhillon et al. 2000) from their accretion disks with a typical accretion rate of $\dot{M} \sim 10^{-10} - 10^{-11} M_{\odot} \text{ yr}^{-1}$, but *no sources in Group B show NIR emission lines*.

This can be reconciled if we assume WD binaries that are not yet recognized as dwarf novae due to absence of the dwarf nova activities. We could also consider other types of WD binaries such as detached WD binaries (Shara et al. 1986; Warner et al. 2003), hibernating CVs, and precursors of CVs called “pre-CVs” (Warner 1995). We hereafter call them all together as “quiet” WD binaries. The “quiet” WD binaries have low accretion mass rates less than $10^{-11} M_{\odot} \text{ yr}^{-1}$. Without dwarf nova activities, these sources are almost indistinguishable from the field main sequence stars in optical and NIR photometric observations. In X-rays, however, some of these sources do show features as WD binaries with $L_X \sim 10^{29} \text{ erg s}^{-1}$ (2–10 keV) and the plasma temperature being $\sim 4 \text{ keV}$ (Matranga

et al. 2012; Schwope et al. 2014), which are typical of Group B sources though the average X-ray luminosity of Group B has a large error. We thus speculate that Group B sources consist mainly of the quiet WD binaries.

To summarize, we suggest that the dominant population of each group as follows: X-ray active stars (Group C), magnetic CVs and non-magnetic CVs with high accretion rates (Group A), and “quiet” WD binaries (Group B). These populations in the groups overlap with each other in figure 9, in which only the X-ray properties are used. The overlap can be disentangled to some extent if we add another axis using NIR property. Figure 10 shows the three-dimensional plot by adding the X-ray to NIR flux ratio. Group A sources tend to have small values along the X-ray to NIR flux ratio, while Group C sources have large values.

4.3 Populations contributing to the GBXE

In previous studies, magnetic CVs and X-ray active stars have been suggested as two most popular groups to explain the GBXE and GRXE. For example, Revnivtsev et al. (2006) discussed the X-ray population based on X-ray luminosity function in the range of $L_X \sim 10^{30} - 10^{32} \text{ erg s}^{-1}$ (2–10 keV) and concluded that the major population constituting the GRXE is

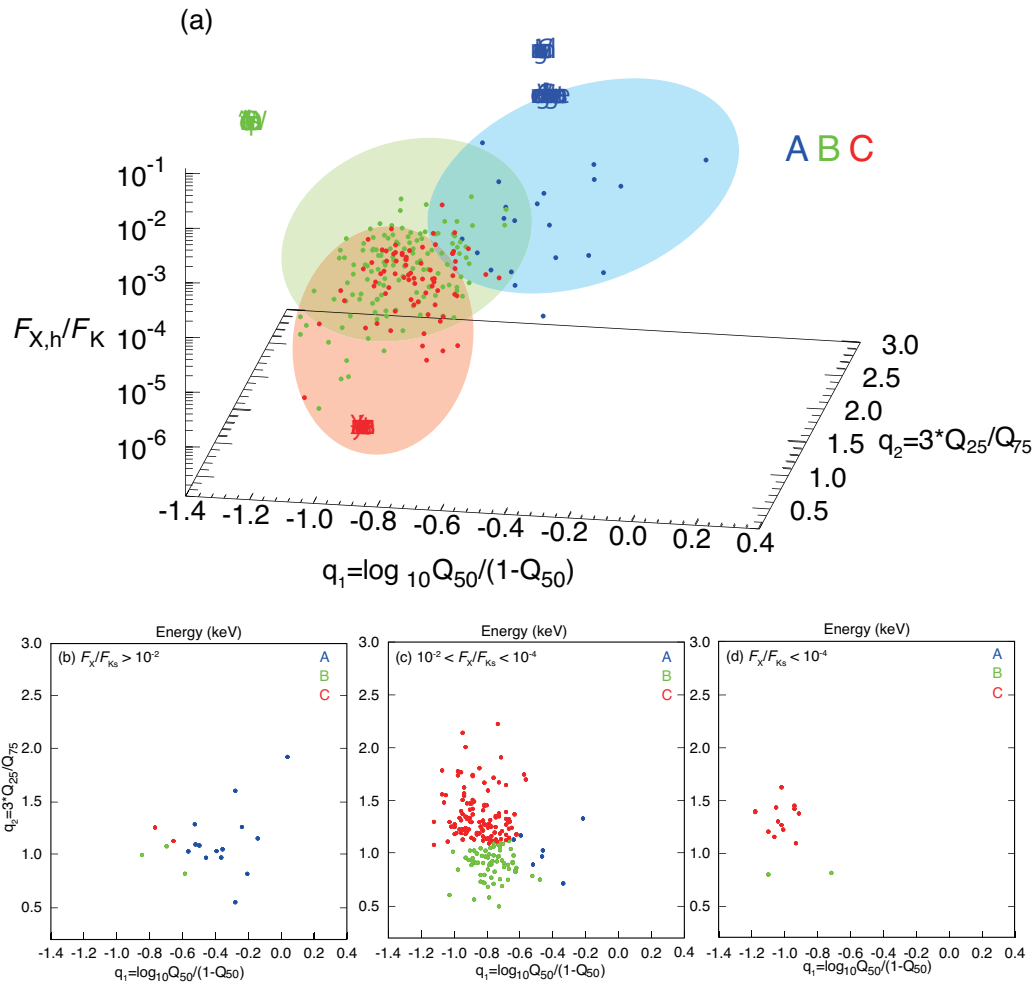


Fig. 10 (a) Three-dimensional plot of q_1 , q_2 , and the ratio of X-ray to NIR flux. Their cross-section on the q_1 - q_2 plane for the ratio of X-ray to NIR flux of (b) $> 10^{-2}$, (c) 10^{-4} - 10^{-2} , and (d) $< 10^{-4}$.

X-ray active binaries, which dominate the population below $L_X \sim 10^{31} \text{ erg s}^{-1}$. Yuasa et al. (2012) constructed a wide-band X-ray spectral model of a type of magnetic CVs (intermediate polars) and fitted it to the 2–50 keV spectra of the GRXE obtained with Suzaku. They argued that the GRXE above 10 keV can be mostly explained by magnetic CVs and that below 10 keV mostly by X-ray active stars. Hong (2012) concluded that the hard X-ray flux above 3 keV is dominant by magnetic CVs and contribution of the X-ray active stars is less than 20%, based on reanalysis of the X-ray data in the CBF.

Most recent studies propose some revisions on these pictures. Though magnetic CVs and X-ray active stars are major populations, there should be other classes of sources that are more dominant. Following the work by Mukai & Shiokawa (1993) based on the X-ray luminosity function, Nobukawa et al. (2016), Yamauchi et al. (2016), and Xu et al. (2016) suggested that non-magnetic CVs should be a more dominant population than magnetic CVs and X-ray active stars. They have reached

this conclusion by comparing the EW, the line ratio, and the scale height of the Fe K line complex between the GRXE and GBXE and the composite X-ray spectra of dwarf novae.

Our results are in line with the conclusions in these recent works in that the dominant contributor to the GRXE and GBXE are non-magnetic CVs. What we claim in this paper is that *the major contributor to the GBXE is quiet WD binaries that are yet to be recognized as dwarf novae*. In fact, such sources are predicted to outnumber the known population of dwarf novae. Theories of CV evolution (e.g., Howell et al. 2001; Hellier 2001; Warner 1995) indicate that CVs remain in the state of low accretion rates for most of their lifetime. An increasing number of such sources are now identified spectroscopically as byproducts of the Sloan Digital Sky Survey and their follow-up studies (Szcodey et al. 2002; 2003; 2004; 2005; 2006; 2007; 2009; 2011). X-ray emission is detected from some of these sources (Reis et al. 2013) with an average X-ray luminosity of as low as $8 \times 10^{29} \text{ erg s}^{-1}$ in the 0.5–10 keV. The luminosity is much

lower than that of typical dwarf novae (Byckling et al. 2010). Reis et al. (2013) further argue that these faint sources are more representative of the WD binaries than those in the brightest end (mostly known as dwarf novae) and that the faint sources account for a significant part of the GRXE. Our findings agree with their claims.

5 Summary

Main results of the present paper are as follows.

1. We carried out a deep NIR JHK_s -band imaging observation at the center of the deep CBF using MOIRCS on the 8.2 m Subaru telescope, and identified $\sim 50\%$ of the X-ray point sources with NIR counterpart candidates. The false positive rate among the identifications is estimated to be 25%. The identification rate increased significantly from our previous NIR survey by using the 1.4 m IRSF telescope in the same field (11%) (Morihana 2012).
2. We classified the X-ray sources into three (A, B, and C) groups based on their X-ray colors. We generated three-dimensional plots (X-ray color-color and the ratio of the X-ray to the NIR flux) to disentangle the overlap among the groups. We have characterized the overall features of each group based on their NIR identification rates, X-ray composite spectra, the flux ratios between the X-ray and NIR bands, X-ray time variability, X-ray average luminosities, and NIR spectroscopy results.
3. Based on the overall characteristics, we argued that the dominant populations of each group are as follows: magnetic CVs and non-magnetic CVs with high accretion rates (Group A), “quiet” WD binaries of low mass accretion rates (Group B), and X-ray active stars (Group C).
4. The composite X-ray spectra of Group B sources have the largest Fe K equivalent width comparable with that of the GBXE. This leads us to speculate that the major constituent of the faint discrete sources for the GBXE is “quiet” WD binaries with low mass accretion rates.

Acknowledgments

We thank Ichi Tanaka for providing the MOIRCS data reduction pipeline as well as useful discussion. We acknowledge the reviewer for useful comments. This work is based on the data collected at Subaru Telescope operated by the National Astronomical Observatory of Japan, public data obtained from Chandra X-ray Center which is operated for NASA by the Smithsonian Astrophysical Observatory, the VVV Survey which is supported by the European Southern Observatory, and the data of the European Space Agency (ESA) space mission Gaia. Gaia data are being processed by the Gaia Data Processing and Analysis Consortium (DPAC). Funding for the DPAC is provided by national institutions, in particular the institutions participating in the Gaia Multi-Lateral Agreement (MLA). IRAF is distributed by the National Optical Astronomy Observatories,

which are operated by the Association of Universities for Research in Astronomy, Inc., under cooperative agreement with the National Science Foundation. This research has made use of SAOImage DS9, developed by Smithsonian Astrophysical Observatory. This work has also made use of software from High Energy Astrophysics Science Archive Research Center (HEASAC) which is provided by NASA Goddard Space Flight Center. K. M. is financially supported by MEXT/JSPS KAKENHI Grant Numbers 17K18019 and 19H01939.

References

- Anders, E. & Grevesse, N. 1989, *Geochim. Cosmochim. Acta*, 53, 197
- Bailer-Jones, C. A. L., Rybizki, J., Fouesneau, M., Mantelet, G., & Andrae, R. 2018, *ApJ*, 156, 58
- Baskill, D. S., Wheatley, P. J., & Osborne, J. P. 2005, *MNRAS*, 357, 626
- Bertinl, E. 1996, *A&AS*, 117, 393
- Byckling, K., Mukai, K., Thorstensen, J. R., & Osborne, J. P. 2010, *MNRAS*, 408, 2298
- Covino, S., Tagliaferri, G., Pallavicini, R., Mewe, R., & Poretti, E. 2000, *A&A*, 355, 681
- Dempsey, R. C., Linsky, J. L., Schmitt, J. H. M. M., & Fleming, T. A. 1993, *ApJ*, 413, 333
- Dhillon, V. S., Littlefair, S. P., Howell, S. B., et al. 2000, *MNRAS*, 314, 826
- Ebisawa, K., Maeda, Y., Kaneda, H., & Yamauchi, S. 2001, *Science*, 293, 1633
- Ebisawa, K., Tsujimoto, M., Paizis, A., et al. 2005, *ApJ*, 635, 214
- Ebisawa, K., Yamauchi, S., Tanaka, Y., et al. 2008, *PASJ*, 60, S223
- Ezuka, H. & Ishida, M. 1999, *ApJS*, 120, 277
- Güdel, M., Linsky, J. L., Brown, A., & Nagase, F. 1999, *ApJ*, 511, 405
- Heard, V. & Warwick, R. S. 2013, *MNRAS*, 434, 1339
- Hellier, C. 2001, *Cataclysmic Variable Stars*
- Hong, J. 2012, *MNRAS*, 427, 1633
- Hong, J., Schlegel, E. M., & Grindlay, J. E. 2004, *ApJ*, 614, 508
- Howell, S. B., Nelson, L. A., & Rappaport, S. 2001, *ApJ*, 550, 897
- Ichikawa, T., Suzuki, R., Tokoku, C., et al. 2006, in *Ground-based and Airborne Instrumentation for Astronomy*, ed. I. S. McLean & M. Iye, Vol. 6269, International Society for Optics and Photonics (SPIE), 397 – 408
- Iso, N., Ebisawa, K., & Tsujimoto, M. 2012, in *American Institute of Physics Conference Series*, Vol. 1427, *Suzaku 2011: Exploring the X-ray Universe: Suzaku and Beyond*, ed. R. Petre, K. Mitsuda, & L. Angelini, 288–289
- Koyama, K. 2018, *PASJ*, 70, R1
- Koyama, K., Ikeuchi, S., & Tomisaka, K. 1986, *PASJ*, 38, 503
- Koyama, K., Maeda, Y., Sonobe, T., et al. 1996, *PASJ*, 48, 249
- Macqueen, J. 1967, *Proceedings of the fifth Berkeley symposium on mathematical statistics and probability*, 1967, 1, 281
- Matranga, M., Drake, J. J., Kashyap, V., & Steeghs, D. 2012, *ApJ*, 747
- Minniti, D., Saito, R. K., Gonzalez, O. A., et al. 2018, *A&A*, 616, 26
- Moorwood, A., Cuby, J. G., & Lidman, C. 1998, *The Messenger*, 91, 9
- Morihana, K. 2012, *PASP*, 124, 1132
- Morihana, K., Tsujimoto, M., Dubath, P., et al. 2016, *PASJ*, 68, 57
- Morihana, K., Tsujimoto, M., Yoshida, T., & Ebisawa, K. 2013, *ApJ*, 766, 14
- Morrison, R. & McCammon, D. 1983, *ApJ*, 270, 119
- Motch, C., Warwick, R., Cropper, M. S., et al. 2010, *A&A*, 523, A92

- Mukai, K. 2017, *PASP*, 129, 062001
- Mukai, K. & Shiokawa, K. 1993, *ApJ*, 418, 863
- Nagayama, T., Nagashima, C., Nakajima, Y., et al. 2003, in *Instrument Design and Performance for Optical/Infrared Ground-based Telescopes*, ed. M. Iye & A. F. M. Moorwood, Vol. 4841 (SPIE), 459
- Nobukawa, M., Uchiyama, H., Nobukawa, K. K., Yamauchi, S., & Koyama, K. 2016, *ApJ*, 833, 268
- Pandey, J. C. & Singh, K. P. 2008, *MNRAS*, 387, 1627
- Pandey, J. C. & Singh, K. P. 2012, *MNRAS*, 419, 1219
- Prusti, T., De Bruijne, J. H., Brown, A. G., et al. 2016, *A&A*, 595, A1
- Reis, R. C., Wheatley, P. J., Gänsicke, B. T., & Osborne, J. P. 2013, *MNRAS*, 430, 1994
- Revnivtsev, M., Sazonov, S., Churazov, E., et al. 2009, *Nature*, 458, 1142
- Revnivtsev, M., Sazonov, S., Forman, W., Churazov, E., & Sunyaev, R. 2011, *MNRAS*, 414, 495
- Revnivtsev, M., Sazonov, S., Gilfanov, M., Churazov, E., & Sunyaev, R. 2006, *A&A*, 452, 169
- Saito, R. K., Hempel, M., Minniti, D., et al. 2012, *A&A*, 537, A107
- Schmitt, J. H. M. M., Collura, A., Sciortino, S., et al. 1990, *ApJ*, 365, 704
- Schwope, A. D., Scipione, V., Traulsen, I., et al. 2014, *A&A*, 561, A121
- Shara, M. M., Livio, M., Moffat, A. F. J., & Orio, M. 1986, *ApJ*, 311, 163
- Skrutskie, M. F., Cutri, R. M., Stiening, R., et al. 2006, *ApJ*, 131, 1163
- Smith, R. K., Brickhouse, N. S., Liedahl, D. A., & Raymond, J. C. 2001, *ApJ*, 556, L91
- Suzuki, R., Tokoku, C., Ichikawa, T., et al. 2008, *PASJ*, 60, 1347
- Szkody, P., Anderson, S. F., Agüeros, M., et al. 2002, *AJ*, 123, 430
- Szkody, P., Anderson, S. F., Brooks, K., et al. 2011, *AJ*, 142, 181
- Szkody, P., Anderson, S. F., Hayden, M., et al. 2009, *AJ*, 137, 4011
- Szkody, P., Fraser, O., Silvestri, N., et al. 2003, *AJ*, 126, 1499
- Szkody, P., Henden, A., Agüeros, M., et al. 2006, *AJ*, 131, 973
- Szkody, P., Henden, A., Fraser, O., et al. 2004, *AJ*, 128, 1882
- Szkody, P., Henden, A., Fraser, O. J., et al. 2005, *AJ*, 129, 2386
- Szkody, P., Henden, A., Mannikko, L., et al. 2007, *AJ*, 134, 185
- Tsuboi, Y., Yamazaki, K., Sugawara, Y., et al. 2016, *PASJ*, 68
- Tsujimoto, M., Kobayashi, N., & Tsuboi, Y. 2005, *AJ*, 130, 2212
- Valinia, A. & Marshall, F. E. 1998, *ApJ*, 505, 134
- van den Berg, M., Hong, J. S., & Grindlay, J. E. 2009, *ApJ*, 700, 1702
- Wada, Q., Tsujimoto, M., Ebisawa, K., & Hayashi, T. 2017, *PASJ*, 69
- Warner, B. 1995, *Cambridge Astrophysics Series*, 28
- Warner, B., Woudt, P. A., & Pretorius, M. L. 2003, *MNRAS*, 344, 1193
- Weisskopf, M. C., Brinkman, B., Canizares, C., et al. 2002, *PASP*, 114, 1
- Wilms, J., Allen, A., & McCray, R. 2000, *ApJ*, 542, 914
- Worrall, D. M., Marshall, F. E., Boldt, E. A., & Swank, J. H. 1982, *ApJ*, 255, 111
- Xu, X.-j., Wang, Q. D., & Li, X.-D. 2016, *ApJ*, 818, 136
- Yamauchi, S., Ebisawa, K., Tanaka, Y., et al. 2009, *PASJ*, 61, S225
- Yamauchi, S., Nobukawa, K. K., Nobukawa, M., Uchiyama, H., & Koyama, K. 2016, *PASJ*, 68, 59
- Yuasa, T., Makishima, K., & Nakazawa, K. 2012, *ApJ*, 753, 129